

An angle-scanned cryogenic Fabry–Pérot interferometer for far-infrared astronomy

Cite as: Rev. Sci. Instrum. **91**, 083108 (2020); <https://doi.org/10.1063/5.0012432>

Submitted: 30 April 2020 • Accepted: 02 August 2020 • Published Online: 20 August 2020

 Ian Veenendaal,  David Naylor, Brad Gom, et al.



View Online



Export Citation



CrossMark

ARTICLES YOU MAY BE INTERESTED IN

[Manufacturing, installation, commissioning, and first results with the 3D low-temperature co-fired ceramic high-frequency magnetic sensors on the Tokamak à Configuration Variable](#)




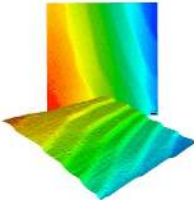

Review of Scientific Instruments **91**, 081401 (2020); <https://doi.org/10.1063/1.5115004>

[A 410 MHz resonant cavity pickup for heavy ion storage rings](#)

Review of Scientific Instruments **91**, 083303 (2020); <https://doi.org/10.1063/5.0009094>

[Calibration of T-shaped atomic force microscope cantilevers using the thermal noise method](#)

Review of Scientific Instruments **91**, 083703 (2020); <https://doi.org/10.1063/5.0013091>

	<p>Nanopositioning Systems</p> 	<p>Modular Motion Control</p> 	<p>AFM and NSOM Instruments</p> 	<p>Single Molecule Microscopes</p> 
---	--	--	---	--



An angle-scanned cryogenic Fabry–Pérot interferometer for far-infrared astronomy

Cite as: *Rev. Sci. Instrum.* **91**, 083108 (2020); doi: [10.1063/5.0012432](https://doi.org/10.1063/5.0012432)

Submitted: 30 April 2020 • Accepted: 2 August 2020 •

Published Online: 20 August 2020



View Online



Export Citation



CrossMark

Ian Veenendaal,^{1,a)}  David Naylor,¹  Brad Com,¹ Adam Christiansen,¹ Willem Jellema,^{2,b)} 
Carolien Feenstra,² Marcel Ridder,³  Martin Eggen,²  and Peter Ade⁴ 

AFFILIATIONS

¹Department of Physics and Astronomy, University of Lethbridge, 4401 University Dr. W, Lethbridge, Alberta AB T1K 3M4, Canada

²SRON Netherlands Institute for Space Research, Landleven 12, 9747 AD Groningen, The Netherlands

³SRON Netherlands Institute for Space Research, Sorbonnelaan 2, 3584 CA Utrecht, The Netherlands

⁴School of Physics and Astronomy, Cardiff University, Cardiff CF24 3AA, Wales, United Kingdom

^{a)}Author to whom correspondence should be addressed: ian.veenendaal@uleth.ca

^{b)}Also at: Kapteyn Astronomical Institute, University of Groningen, Landleven 12, Groningen 9747 AD, The Netherlands.

ABSTRACT

The sensitivity of state-of-the-art superconducting far-infrared detectors used in conjunction with cryogenically cooled space telescopes and instrumentation is such that spectroscopic observations are generally limited by photon noise from the astronomical source or by galactic foreground or zodiacal emission within the field-of-view. Therefore, an instrument design that restricts the spectral bandpass viewed by the detector must be employed. One method of achieving background limited, high resolution spectroscopy is to combine a high resolution component such as a Fabry–Pérot interferometer (FPI) with a lower resolution, post-dispersing system, such as a grating spectrometer, the latter serving to restrict the spectral bandpass. The resonant wavelength of an FPI is most often tuned by changing the spacing or medium between the parallel reflecting plates of the etalon. In this paper, we present a novel design for an FPI in which the wavelength is tuned by scanning the angle of incidence on a high refractive index etalon. This concept simplifies the cryomechanical design, actuation, and metrology. The first results from the realized instrument are presented and compared with theory. The effects on the spectral response as a function of the incident angle have been simulated and shown to agree well with the observation.

Published under license by AIP Publishing. <https://doi.org/10.1063/5.0012432>

I. INTRODUCTION

The Space Infrared Telescope for Cosmology and Astrophysics (SPICA) is a collaboration between the European Space Agency (ESA) and the Japan Aerospace Exploration Agency (JAXA).¹ This observatory class mission will provide mapping, spectroscopic, and polarimetric capabilities within the 12 μm –350 μm wavelength range with a 2.5 m telescope cooled to a temperature less than 8 K through a combination of passive cooling and mechanical coolers. The SPICA Far-infrared Instrument (SAFARI) is one of the three onboard instruments that will, in combination with a new generation of ultra-sensitive far-infrared detectors (NEP $\sim 10^{-19}$ W/ $\sqrt{\text{Hz}}$) and a cold telescope, allow astronomers to achieve spectroscopic

observations with sky-limited sensitivity over the 34 μm –230 μm wavelength range. To realize this goal, however, a dispersive spectrometer based on a diffraction grating is required so that each detector observes a limited spectral band chosen such that the photon noise from the astronomical source in this band is comparable to the readout noise to optimize the sensitivity of the instrument. Since a diffraction grating spectrometer provides only low resolution spectroscopy, a complementary high resolution component is required to resolve narrower astronomical spectral features. In this paper, we present the design of a novel Fabry–Pérot interferometer (FPI) concept developed as a potential high resolution spectrometer solution. Although an alternative solution based on a Martin–Puplett Fourier transform spectrometer² (MP-FTS) has been adopted as the baseline

for SAFARI, the instrument concept presented here could be utilized in future missions.

II. BACKGROUND

In the case of an ideal, plane parallel FPI illuminated by a plane wave, the transmitted electric field may be expressed as a geometric series that coherently sums each intermediate transmitted beam, shown in Fig. 1. Assuming beam divergence is negligible, and the area of each intermediate beam in the series is identical, the resulting series is³

$$E_T = E_0 t_1 t_2' \sum_{m=0}^{\infty} (r_1' r_2')^m e^{im\delta} = \frac{E_0 t_1 t_2'}{1 - r_1' r_2' e^{i\delta}} \quad (\text{V m}^{-1}), \quad (1)$$

where t_n and r_n are the Fresnel transmission and reflection amplitude coefficients for the n th boundary between the etalon and the environment, with the primed coefficients denoting boundary interactions within the etalon, and δ is the phase difference between consecutive interfering beams. The phase difference depends on the wavelength λ , the etalon thickness d , the refractive index n , and the transmitted beam angle θ_t by

$$\delta = \left(\frac{2\pi}{\lambda}\right) 2nd \cos \theta_t. \quad (2)$$

Additionally, θ_t is related to the angle of incidence θ by $\sin \theta = n/n_0 \sin \theta_t$. Note that optical losses within the etalon substrate may be accounted for by inclusion of an imaginary component of the refractive index n .

The transmitted intensity is proportional to the squared modulus of the sum of the transmitted electric fields, and is given by the Airy function.⁴ Assuming both surfaces of the etalon are identical, the reflection and transmission amplitude coefficients can be expressed in terms of the total intensity reflection and transmission, R and T , and the expression for the transmitted intensity as a function of the incident intensity I_0 becomes

$$I_T = \frac{T^2}{(1-R)^2} \frac{I_0}{1 + \left[\frac{4R}{(1-R)^2}\right] \sin^2(\delta/2)} \quad (\text{W m}^{-2}). \quad (3)$$

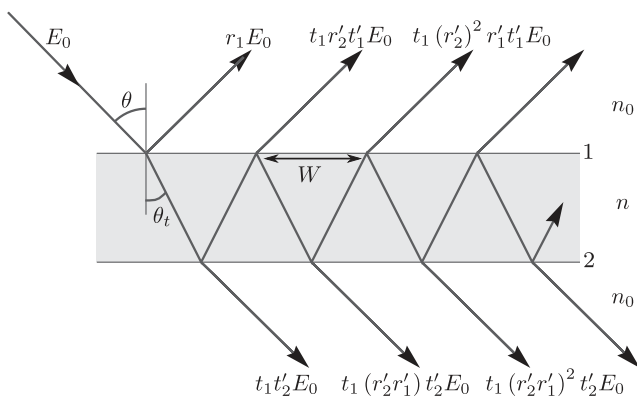


FIG. 1. A diagram of the beam paths at the etalon interfaces. The terms at each beam represent the relative E-field in terms of the incident field E_0 . The variable definitions and phase delay within the etalon are described in the text.

The transmitted intensity varies with the parameter δ , from which it can be seen that the resonant wavelength of the FPI can be scanned by varying d , n , or θ ; by far, the most common approach is to vary the spacing d .⁵

In this paper, we present the design of a cryogenic FPI, shown schematically in Fig. 2, based on scanning the angle of incidence, θ . A monolithic pendulum scanning mechanism, which incorporates two precision, diamond turned plane mirrors, with an internal angle of 90° , directs light through the etalon, which is mounted at a pupil image and at an offset angle of 15° to allow single sided scans of the etalon with a scan range of $\pm 7^\circ$.

The principal advantages of the angle-scanned design are that the motion is only required around one axis, which simplifies both the actuation and metrology, and that the etalon itself can be fabricated plane and parallel by design, obviating the need to maintain parallelism of the etalon plates if the gap, d , was to be scanned. For example, this design requires significantly less resources for its operation than the FPI in the ISO LWS/SWS instrument,⁵ which is important in cryogenic application at 4 K, where thermal budgets are limited.

The principal disadvantage of this design is that the multiply reflected beams suffer increasing walk-off of the finite etalon aperture as the angle of incidence increases. The effect of walk-off is to change the spectral response as a function of angle, or effectively wavelength, as the number of interfering beams decreases with increasing θ . In the case of m interfering beams, ignoring differing aperture effects for each interfering beam, the above equation is modified to⁶

$$I_T = \frac{I_0(1-R^m)^2}{1 + \left[\frac{4R}{(1-R)^2}\right] \sin^2\left(\frac{\delta}{2}\right)} \times \left\{ 1 + \left[\frac{4R^m}{(1-R^m)^2}\right] \sin^2\left(\frac{m\delta}{2}\right) \right\} \quad (\text{W m}^{-2}). \quad (4)$$

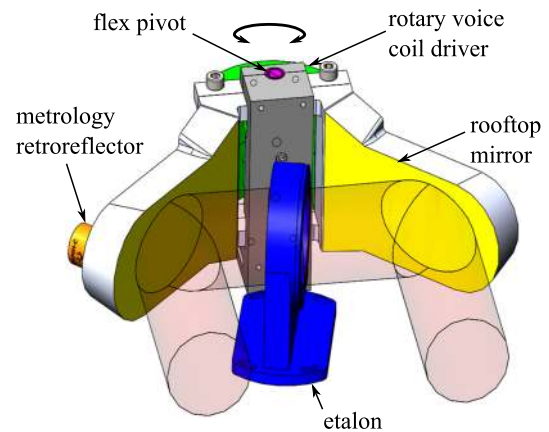


FIG. 2. FPI schematic in which the angle of incidence on the offset mounted etalon (blue) is scanned as the rooftop mirror pendulum, actuated by opposing rotary voice coil drivers (green), rotates about the pivot (purple). A corner cube retroreflector (orange) mounted to the rear of the pendulum arm forms a part of a cryogenic laser metrology system to determine θ . A schematic that shows the optical beam passing through the etalon is shown in Fig. 9.

The term outside of the braces shows the reduction in peak transmitted intensity due to walk-off, and the part of the equation in braces describes the broadening of the intensity profile with decreasing m . The number of round trips can be determined by finding the lateral shift, W , in the beam for each pass through the etalon as follows (Fig. 1):

$$W = 2d \tan \theta_t \quad (m), \quad (5)$$

where θ_t is the internal angle of the beam with respect to the etalon normal and d is the etalon thickness. In the case of a finite aperture, the transmitted cross-sectional area of each beam drops as the area overlap between the beam and the aperture decreases due to beam walk-off. With an aperture stop of diameter D_c , only the overlapping area with each beam within the aperture contributes to interference. If we define the relative walk-off, $w = W/D_c$, and the total number of round trips before the beam completely leaves, the aperture becomes $M = 1/w$ (Fig. 3). By ensuring the etalon diameter at maximum tilt angle is not the limiting aperture of the optical system, the beam cross section retains circular symmetry, and after m round trips, the overlapping area fraction with the original aperture can be written as⁷

$$f(m) = \frac{2}{\pi} \left[\cos^{-1}(mw) - mw \sqrt{1 - (mw)^2} \right]. \quad (6)$$

Incorporating the relative area overlap between successive transmitted beams, the amplitude of the m -th transmitted wave is weighted by a factor $\sqrt{f(m)}$. The total transmission becomes⁷

$$T_{\text{FPI}}(\theta_t, \lambda) = T^2 \left| \sum_{m=0}^M R^m e^{im\delta} \sqrt{f(m)} \right|^2. \quad (7)$$

To avoid the added complexity introduced by walk-off, historically Fabry–Pérot interferometers have been operated at normal incidence. However, with modern computing power, the challenges of calibrating an angle-scanned etalon, which requires a unique correction for each angle of incidence, are considered manageable.

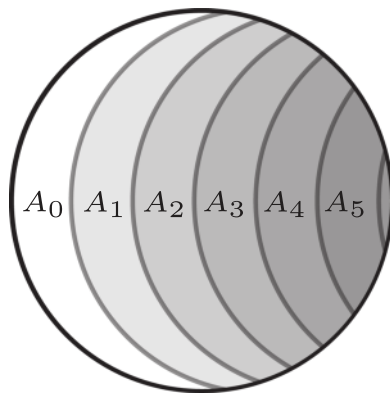


FIG. 3. Schematic of the impact of walk-off on the overlapping area between transmitted beams. The effect of walk-off is exaggerated to show the diminishing beam area overlap for each successive reflection.

III. SIMULATING THE EFFECTS OF WALK-OFF

The finesse, \mathcal{F} , of a Fabry–Pérot interferometer is defined as the ratio of the free spectral range to the full width at half maximum (FWHM) of the spectral response function. In the ideal case, the finesse is dominated by the reflectivity finesse, which is given by⁴

$$\mathcal{F} = \frac{\pi\sqrt{R}}{1 - R}. \quad (8)$$

Finesse is a useful metric, which represents the increase in resolving power that will be achieved when an FPI is used in conjunction with a post-dispersive element, whose resolution element matches the free spectral range of the FPI.³

Figure 4 shows the simulated effect of walk-off for an angle-scanned, air/vacuum gap etalon designed to provide a finesse of ~ 10 at a wavelength of $260 \mu\text{m}$. These values are chosen to mimic the SAFARI application in which the grating alone provides a resolving power, $\mathcal{R} \sim 300$ and in conjunction with the FPI, $\mathcal{R} \sim 3000$. In this simulation, the air gap etalon is formed using inductive metal mesh grids. The reflectivity of each grid is individually simulated to infer reflectivity, R .⁸ An air gap of 27 mm is required to achieve the desired resolving power, and an incident angular scan range of 5° is required to cover a full spectral order. It can be seen that the change in spectral response as a function of wavelength for an etalon aperture of 40 mm due to walk-off is severe.

Figure 5 shows the simulated effect of walk-off for an angle-scanned etalon formed by mounting a dielectric mirror in the form of an air gap layer followed by a silicon layer ($\sim 60 \mu\text{m}$ each) on either side of a high resistivity (HRFZ) silicon substrate of thickness 8 mm (Fig. 7). While the high refractive index of the substrate partly mitigates the effects of walk-off, the angle scan required to achieve the target wavelength range is scaled by the refractive index of the silicon substrate to $>17^\circ$. It can be seen that the resulting variation in spectral response as a function of wavelength has been significantly

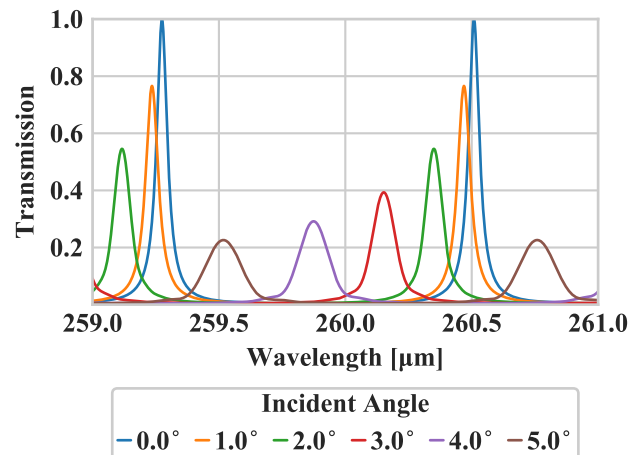


FIG. 4. Simulated transmission as a function of wavelength for an air gap (27 mm) etalon employing inductive metal mesh reflectors. The etalon has a clear aperture of 40 mm at normal incidence and the scan range is 0° – 4.8° , corresponding to two etalon orders. The effect of walk-off is clearly evident.

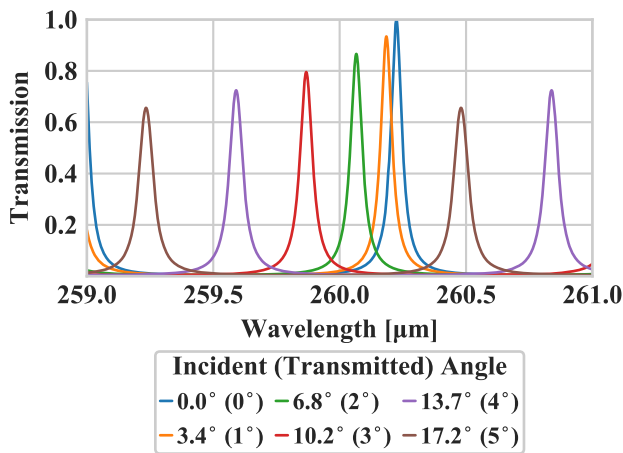


FIG. 5. Simulated transmission as a function of wavelength for an etalon made from a high resistivity silicon slab (8 mm) between air gap/silicon dielectric mirrors. The effect of walk-off is seen to be less severe, however, absorption within the silicon substrate has not been included in this analysis, and the incident angle scan range has increased from Fig. 4.

improved. However, the effect of absorption within the high resistivity silicon substrate has not been included in this analysis. While the loss tangent of HRFZ silicon is expected to be very low at terahertz frequencies ($<10^{-5}$), it has not been well characterized at cryogenic temperatures. Indeed, one of the best ways of determining the loss tangent is by constructing and measuring the transmission of a high finesse silicon Fabry-Pérot etalon.

Volume is a key driver for cryogenic space instrumentation and Fig. 5 shows the benefit of employing an etalon having a high refractive index substrate in an angle-scanned FPI configuration; in this example, the gap has been reduced from 27 mm to 8 mm. Furthermore, with the diminished effects of walk-off, it becomes useful to

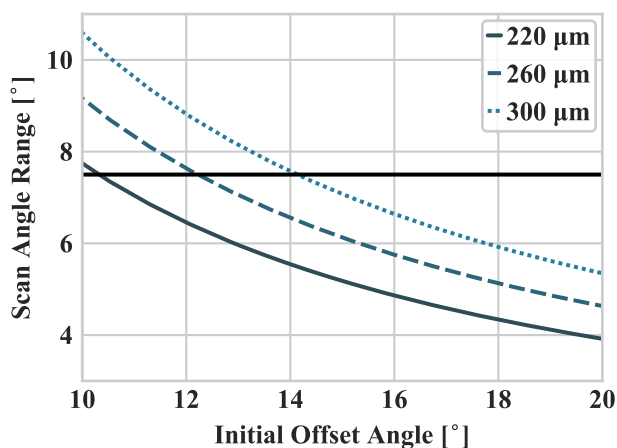


FIG. 6. The semi-angle scan range that is required to cover a full spectral order is shown as a function of the initial offset angle of the etalon with respect to the optical axis. The solid black line indicates the $\pm 7.5^\circ$ limitation imposed by the chosen flexures.

perform a trade-off between the initial offset angle of the etalon with respect to the optical axis, and the angular tilt range required to scan a full spectral order. Because of the cosine dependence, for a larger offset angle, a smaller angular scan range is required (Fig. 6). For our specific case, we procured cryogenic flexure bearings with a $\pm 7.5^\circ$ scan range,⁹ for which the minimum offset angle was required to be no less than 15° to cover the full designed wavelength range. These flexures were chosen because they had cryogenic space flight heritage,¹⁰ being used as part of the focal plane chopper unit of the HIFI instrument on the Herschel Space Observatory.¹¹

IV. ETALON DESIGN

An etalon requires high-reflectivity surfaces to achieve high resolving power. Finding materials that exhibit both high reflectivity and low absorption in the FIR region is a considerable challenge. Since reflectors made from metal deposited on a dielectric are either too thin to reflect effectively or too thick resulting in significant absorption, other materials are required. Historically, FIR reflectors have been developed from thin metallic mesh structures deposited on thin Mylar sheets.⁸ This type of reflector can also be fabricated without the substrate resulting in free-standing meshes. This approach was adopted for the air gap scanned Fabry-Pérot interferometers of the short (SWS) and long (LWS) wavelength spectrometers of the Infrared Space Observatory (ISO).¹² However, as shown in Fig. 4, the effects of walk-off in the case of a small aperture and large air gap precluded their use in a high resolution angle-scanned concept.

To address the walk-off issue, two etalon designs were considered, both based on the use of a high refractive index silicon substrate. The first approach was a hybrid etalon consisting of reflective metal meshes of the ISO LWS heritage mounted on thin invar rings to create a small air gap ($\sim 10 \mu\text{m}$) on either side of a high refractive index HRFZ silicon substrate. The second approach was to use etching and micromachining techniques to develop a fully

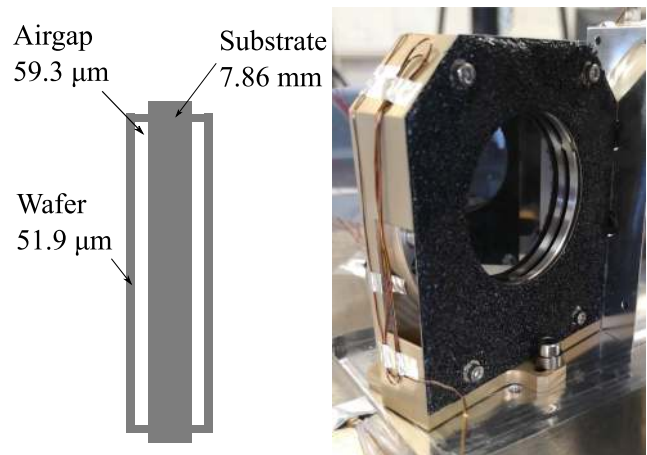


FIG. 7. Left: Cross section of the etalon showing the wafer-air gap-substrate-air gap-wafer structure (not to scale). Vent holes (not shown) allow the air gap to be evacuated. Right: The silicon etalon within the cryogenic mount shown with absorber panels to reduce the effects of stray light.

TABLE I. Etalon design specifications.

Parameter	Minimum	Nominal	Maximum
Wavelength (μm)	220	240	300
Diameter (OD) (mm)		50.8	
Clear aperture (ID) (mm)		44	
Beam diameter (mm)		40	
Refractive index		3.4	
Thickness (mm)		7.86	
Angle of incidence (AoI) (deg)	0°	15°	22°
Finesse	6	23	35
FSR (μm)	0.96	1.0	1.8
Spectral resolving power	1000	5000	8000

silicon-based etalon (Fig. 7). Thin silicon wafers were attached to the substrate with an air gap between the wafer and substrate to form dielectric stacked coatings, which mimic high reflectivity for narrow wavelength bands by utilizing constructive interference on multiple reflections (the principle on which the etalon itself functions). While the first approach appeared the easiest, the task of mounting three different components, with different coefficients of thermal expansion (CTEs), proved to be difficult. At the same time, significant advances were being made in the techniques required to fabricate the fully silicon etalon. As a result, the latter approach was adopted as our chosen solution.

Thin HRFZ Si wafers were first ground and polished to an appropriate thickness to form the reflecting surfaces. The wafers contained an etched air gap, which included a support ring with venting holes to evacuate the air gap for cryogenic, vacuum operation, and were epoxied to the silicon substrate to provide an air gap between the wafer and the substrate. The procedure was repeated on both faces of the etalon substrate. In this way, a H/L/H dielectric stack on both sides of the etalon was achieved to provide high reflectivity. The dielectric stack coating on the etalon was designed such that the path length difference between reflections from the outer surface of the wafer and from the substrate were twice the design wavelength of 240 μm at normal incidence. This was expected to provide a good compromise between structural stiffness and ease of

manufacturing. A schematic of the etalon is shown in Fig. 7 together with an image of the manufactured etalon within its cryogenic mount. Complete details of the etalon fabrication process will be described by the authors in a future publication. The etalon mount consisted of an aluminum bracket using spring gaskets to compensate for differences in CTE, avoiding unacceptable stresses in the silicon substrate, and creating a conductive thermal path between the substrate and the 4 K cold plate. The temperature of the etalon was monitored using a temperature sensor which was directly mounted on the edge of the silicon substrate.

The effective reflectivity of the etalon was modeled, for both *s*- and *p*-polarizations, and as a function of the incident angle, using the multiplication of transfer matrices for the consecutive optical interfaces. The etalon design specifications are presented in Table I.

V. ANGLE-SCANNING FPI DESIGN

An overview of the integrated FPI system is shown in Fig. 8. To calibrate the FPI, a custom-built THz photomixer is illuminated by two tunable continuous-wave (CW) infrared lasers, providing a continuously tunable, CW narrow-line emission source at the difference frequency between the lasers.¹³ Alternatively, a gas cell can be placed in front of the instrument to superimpose narrow absorption lines on a background continuum source, to provide an absolute wavelength calibration.

The beam from the source optics is directed into a large test facility cryostat so that its focus lies on the entrance slit to the spectrometer, which is mounted to the 4 K plate.^{14,15} Thermal filters are placed in this converging beam, on the vacuum chamber, and on the first and second stage radiation shields to minimize contributions from stray light. Beyond the entrance slit, a collimator and plane mirror direct the beam toward the rooftop mirror of the pendulum assembly shown schematically in Fig. 9. With the etalon placed between the pivoting rooftop mirror, the incident angle of the beam on the etalon can be changed without affecting the beam geometry outside of the rooftop. The etalon is mounted at an offset angle, which can be adjusted and optimized to provide an adjustable angular scan range for a given free spectral range (Fig. 6). The etalon

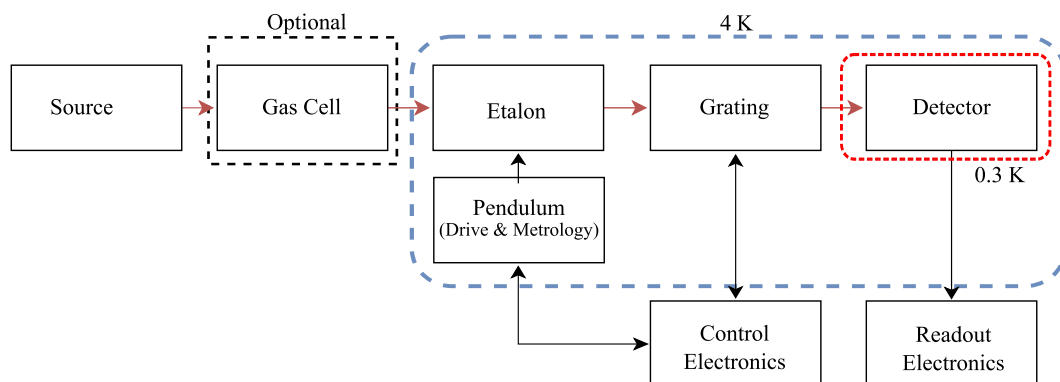


FIG. 8. System level block diagram for the angle scanned FPI.

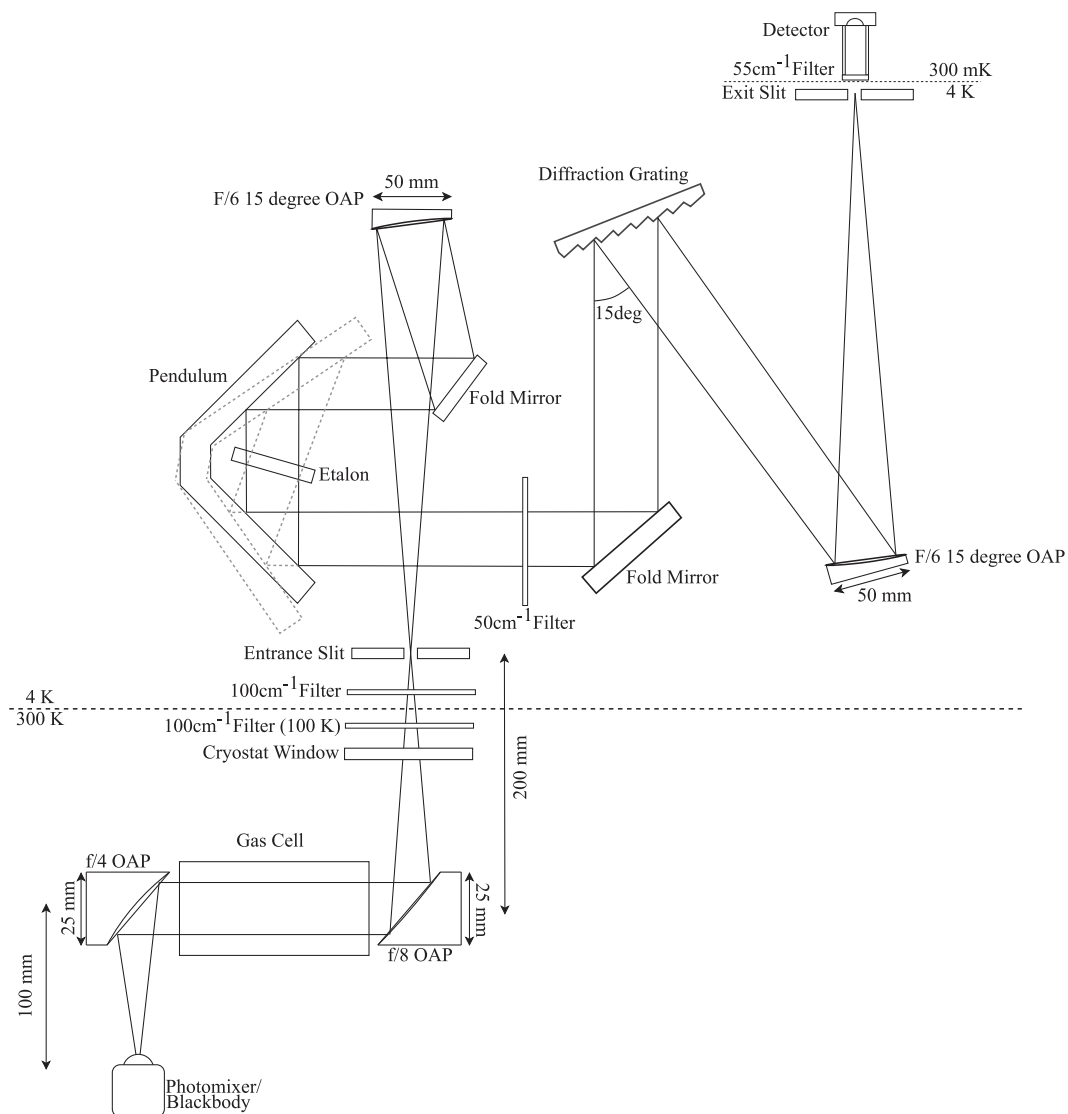


FIG. 9. Sketch of the optical layout for the integrated FPI. OAP refers to an off-axis parabolic mirror. The schematic shows two positions of the pendulum, highlighting the change in beam angle with respect to the etalon. Since the pendulum pivots about the apex defined by the rooftop mirror, the output beam location does not change.

holder contains absorbing panels that serve to mitigate the effects of stray light and provide an aperture stop for the optical system. Beyond the rooftop, exiting to the lower right in Fig. 9, the beam is directed through a fourth filter mounted on the entrance aperture of the custom designed, scanning grating spectrometer that serves as an order sorter for the FPI. The cryogenic grating spectrometer is of the Czerny–Turner configuration¹⁶ whose output is brought to a focus on an exit slit behind which is located a sensitive 300 mK composite bolometer detector.¹⁷ A cryogenic stepper motor,¹⁸ flexibly coupled to a worm and wheel reducing gear, enables rotation of the grating to select the spectral bandpass. The grating specifications are given in Table II.

VI. RESULTS

The first step in validating the performance of the angle scanned FPI was to confirm that the resolving power of the grating spectrometer was sufficient to order sort the higher resolution FPI. With the etalon removed and the grating held at a fixed angle, the photomixer was tuned across the grating bandpass. To first order, the spectral response of the grating is expected to be Gaussian. The upper plots in Fig. 10 show typical results of fitting a Gaussian function to the raw data, which confirms that both the spectral response and the target resolving power of ~ 300 were achieved. The lower plot in Fig. 10 compares the observed center of the grating response as a

TABLE II. The specifications for the grating used to order sort the FPI. The deviation angle, 2ϕ , between incident and diffracted beams remains constant in the Czerny–Turner monochromator configuration. The exit focal length requires an $\sim f/6$ optic.

Parameter	Value
Height	100 mm
Width	50 mm
Order	1
Spacing	180 μm
2ϕ	15°
Blaze	47°
Focal length	310 mm
Exit slit width	2 mm

function of the grating angle with theory, establishing the grating spectral calibration.

Once the grating had been calibrated, the etalon was installed between the arms of the pendulum as shown schematically in Fig. 2 and in Fig. 11.

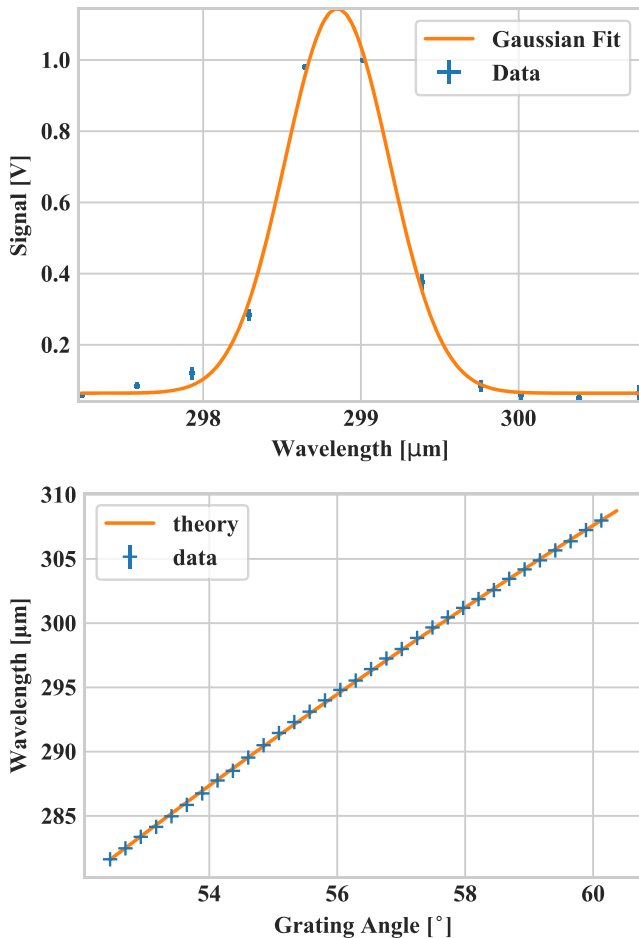


FIG. 10. Upper: A Gaussian fit to a grating spectral response measurements. Lower: Relation between the grating angle and center wavelength determined from fits to the individual response functions and comparison with theory.

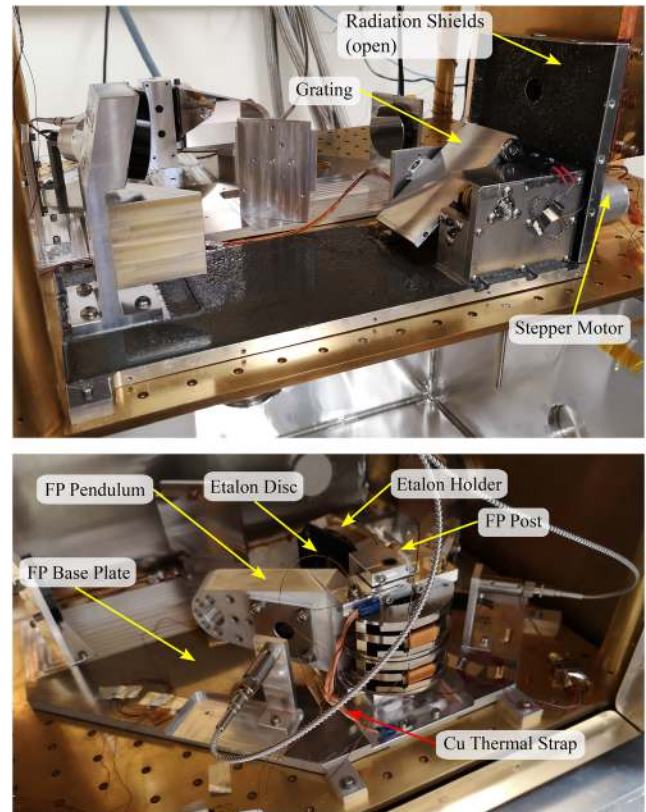


FIG. 11. Images of the experimental setup of the FPI and grating modules within the 4 K enclosure.

The spectral calibration of the FPI was based on the spectral response of the instrument when observing the narrow, unresolved line produced by the photomixer.¹³ With the grating held fixed, the output wavelength of the photomixer was stepped through the predicted grating profile and data collected from several (~ 5) micro-scans of the pendulum. The transmission function of the FPI was obtained by stitching together the individual spectral micro-scans.

Five parameters were required to model the performance of the FPI: the substrate thickness, the wafer thickness, the air gap between the wafer and the substrate, the refractive index of silicon at 4 K, and the angle of incidence. The thickness and gap parameters were obtained by a coordinate measurement machine during the manufacturing process. Moreover, the thermal contraction of silicon has been well characterized at cryogenic temperatures.¹⁹ Using the recorded temperatures of the thermometers attached to the edges of the silicon substrate, the thickness of the substrate at the operating temperature was determined. Additionally, the temperature of the silicon at the etalon edge was stable and we did not observe a temperature dependence on the photomixer power output. As a result, we concluded that the thermal gradients across the etalon were negligible, although we could not measure this directly.

The refractive index of silicon at these wavelengths and the initial offset angle of the etalon were the only variables in the model fit. While the refractive index of silicon as a function of temperature is well known at near infrared wavelengths,²⁰ and some publications report far infrared values at room temperature and 1.5 K,²¹ the precise dependence of refractive index on temperature dn/dT is not well characterized at far infrared wavelengths. Although the refractive index of silicon also exhibits a frequency dependence, this effect was modeled as negligible over the measured frequency range compared to the expected measurement precision. Another concern is that, since high resistivity silicon is a poor thermal conductor, the temperature near the center of the etalon may be higher than the measurement provided by the thermometers located on the edge of the substrate. For these reasons, we allowed the refractive index to be a free parameter in our fit. While the precision of the laser based cryogenic metrology system has been measured to be ~ 2 nm rms,²² resulting in an angular precision of $0.007''$, the absence of a fiducial marker in these first scans led to an uncertainty in the initial angle of incidence. For this reason, the initial offset angle was also allowed to vary in the fitting procedure.

The calibration scheme that was adopted for the FPI was based on the average measurement obtained from the forward and reverse scans of the pendulum, and an estimated initial offset of $(15 \pm 1)^\circ$ was determined by the design offset and mechanical tolerances. For each input wavelength, a number of selected refractive indices were applied to the multilayer model to generate model outputs. The angle at which the peak transmission in the model occurred was found and the difference in the initial offset angle was calculated. The refractive index was taken to be the values that minimized the variance in offset angles for all mini-scans, regardless of the angle at which the transmission peak occurred (Fig. 12). Using this method, the optimum refractive index and initial angle of incidence were determined and the details are given in Table III. The measured refractive

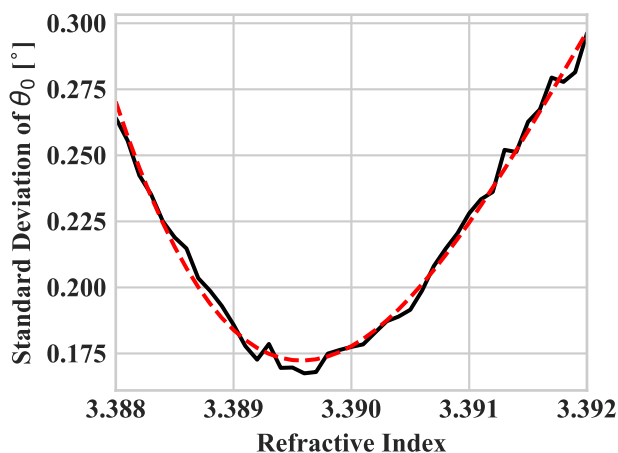


FIG. 12. Visualization of the minimization of the variance in the offset angle for the calibrated wavelength range. A fourth-order polynomial fit is overlaid, which is used to find the optimum refractive index. From extrapolation from near-infrared cryogenic measurements, the refractive index was expected to be ~ 3.39 .

TABLE III. Parameters of the etalon which were used for wavelength calibration.

Parameter	Value
Substrate thickness	(7.860 ± 0.001) mm
Air gap thickness	(59.3 ± 0.1) μ m
Wafer thickness	(51.9 ± 0.1) μ m
Refractive index	3.390 ± 0.001
Offset angle	$(15.0 \pm 0.2)^\circ$

index matches well with extrapolated near-infrared and cryogenic measurements.^{20,21}

Having established the calibration parameters for the angle scanned FPI spectra were subsequently obtained over the wavelength range from $280 \mu\text{m}$ to $320 \mu\text{m}$. Figure 13 shows a sample of four independent spectral line measurements. Each plot was obtained by first selecting a grating angle and thus central wavelength (Fig. 10) and tuning the photomixer output to this wavelength. The incident beam angle was varied across the etalon with slow periodic scans of the pendulum angle. The average signal from ten forward and reverse scans of the pendulum was computed as a function of angle. The resulting spectral line profiles were compared to two models: the first of which computed the transmission through the etalon assuming the etalon was an infinitely wide stack of dielectric layers, and the second incorporated the effects of walk-off due to the finite aperture between the reflective layers on either side of the etalon substrate. Both models show excellent agreement with the collected data, indicating that the effects of walk-off on the shape of the spectral line profile were small for the resolving powers of the etalon at these wavelengths. Although, as the residual in the upper left plot in Fig. 13 shows, the discrepancy between models became more pronounced at shorter wavelengths.

Naturally, with increasing resolving power, the effects of walk-off are expected to become more prominent. In general, the model that included the effects of walk-off showed a slightly better agreement with the measured data. Figure 14 shows a linear fit of the normalized rms deviations for each model over all measured wavelengths. While the deviations fell below the noise in each measured line profile, and therefore were widely varying between scans, the general trend showed an improvement in the fit quality by including the effects of walk-off. We can conclude that the walk-off model captured the subtle effects of the broadening of the instrumental line function. In particular, when a region between the transmission peaks was scanned, the importance of including the effects of walk-off was immediately evident as shown in Fig. 15.

While the etalon was designed to provide optimum performance at wavelengths between $220 \mu\text{m}$ and $300 \mu\text{m}$, the available power from a THz photomixer, which varies as λ^4 , quickly became the limiting factor in obtaining the high signal-to-noise measurements necessary to study the line profiles in detail. Despite this limitation, by tuning the difference frequency between the ($\sim 1.55 \mu\text{m}$) distributed feedback (DFB) lasers that illuminate the photomixer, thus altering the output frequency, we were able to compare the measured and theoretically predicted resolving power over the wavelength range $280 \mu\text{m}$ – $320 \mu\text{m}$.

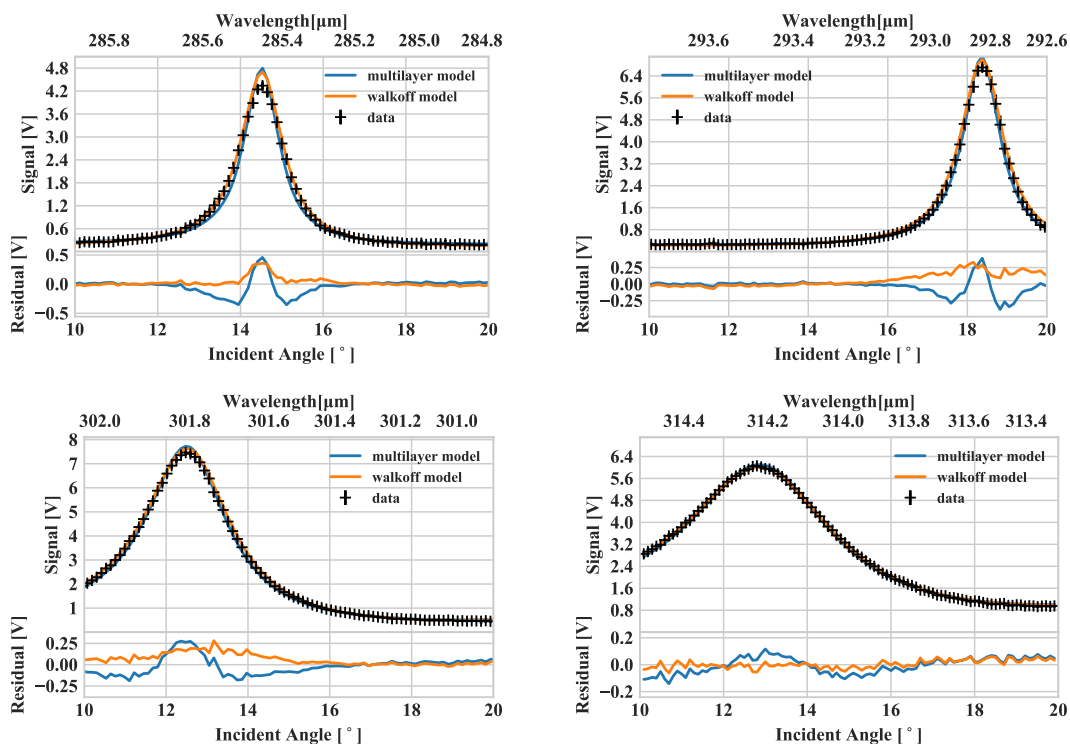


FIG. 13. Line profiles obtained during the spectral calibration of the FPI for photomixer wavelengths of 285.5 μm , 292.8 μm , 301.8 μm , and 314.2 μm . The figures show the incident beam angle on the lower x-axes and the corresponding wavelength scale on the upper x-axes. Each dataset was fit with two models: the multilayer model determined the transmission by solving for the electric field at all boundaries of the etalon; the walk-off model determined the reflection coefficients for the front and back etalon surfaces as a function of wavelength and angle, and included the diminishing area overlap from beam walk-off within the etalon. The residuals between each model and the data are shown underneath each figure.

The resolving powers determined from fits to the individual line profiles yield values of ~ 2000 at 280 μm (Fig. 16), consistent with the design goals for the angle-scanned Fabry–Pérot interferometer of achieving resolving powers of >5000 at 220 μm . Note that

the spread in measured resolving powers in Fig. 16 was due to slow temperature drifts in the infrared lasers, which we were not able to continuously monitor. Additionally, the presence of a strong water vapor transition near 305 μm skew the measured line width in that region.

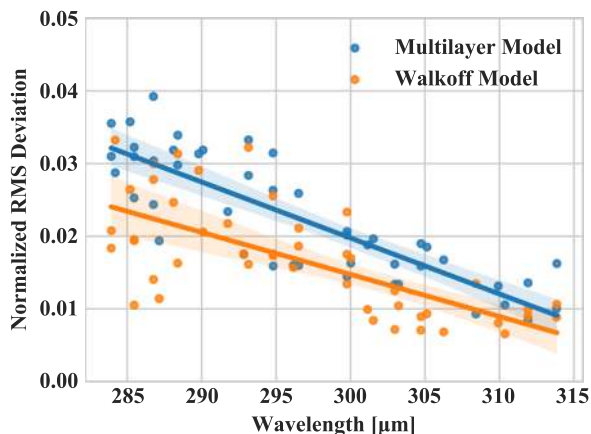


FIG. 14. Comparison between the normalized rms deviations between the model and data for the multilayer model and the walk-off model. A linear fit is performed for the deviation in each model to show the quality of the model as a function of wavelength, and the relative improvement of the model by incorporating the walk-off method.

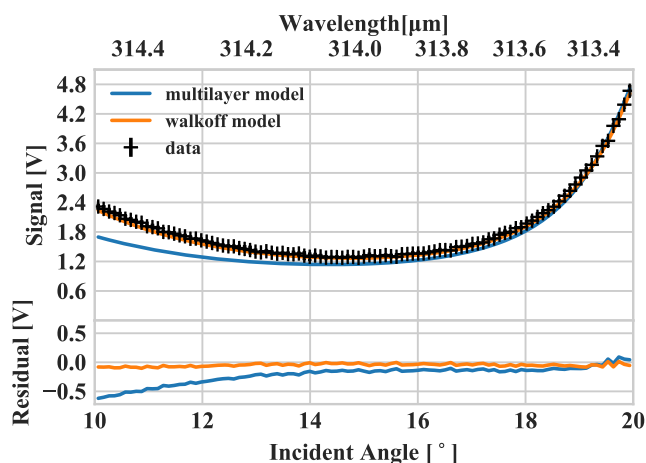


FIG. 15. An FPI scan that falls between two transmission peaks. The walk-off model expects a transmission profile with slightly broader lines, and is therefore able to provide a better fit to the sidelobes of the line profile.

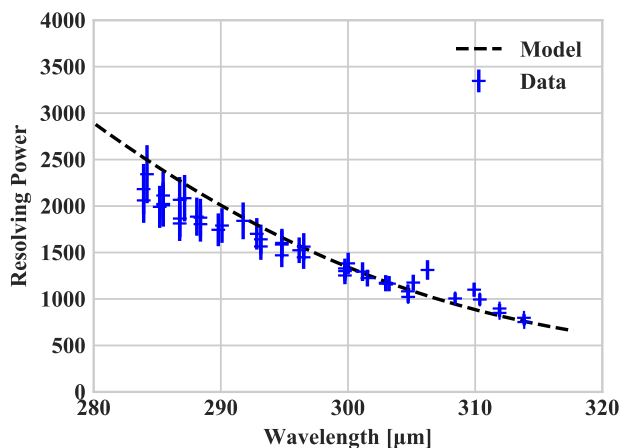


FIG. 16. Comparison of the measured resolving power (blue crosses) with theoretical resolving power as determined by the multilayer etalon model including walk-off.

In summary, these first results from a novel cryogenic angle-scanned Fabry–Pérot interferometer show that the effects of walk-off and potential absorption losses have not compromised the performance of the custom-designed etalon at the target resolving powers.

VII. CONCLUSION

In this paper, we presented a novel design for a cryogenic Fabry–Pérot interferometer in which the wavelength was tuned by scanning the angle of incidence on a high refractive index etalon. This concept simplifies the cryomechanical design, actuation, and metrology. The effects on the spectral response of the varying angle of incidence have been simulated and shown to agree well with the observation. These results showed the first implementation of a cryogenic, angle scanned FPI etalon as a high-resolution spectroscopic instrument.

ACKNOWLEDGMENTS

The authors would first like to thank Trevor Fulton for his assistance with providing detailed modeling for the Fabry–Pérot etalon as well as Rebecca Sirota for her technical support in developing control and readout hardware for the photomixer source and the laser metrology readout. Also, they would like to thank Rik ter Horst for his efforts in the grinding, polishing, and preparation of the silicon wafers. Additionally, the authors would like to thank the funding agencies that supported this project: the Canadian Foundation for Innovation (CFI), the Canadian Space Agency (CSA) through the Flights and Fieldwork for the Advancement of Science and Technology (FAST) funding initiative, the Natural Sciences and Engineering Research Council of Canada (NSERC), and Blue Sky Spectroscopy Inc. Ian Veenendaal is a recipient of the NSERC Alexander Graham Bell Canadian Graduate Scholarship, and the Alberta Innovates Technology Futures Graduate Scholarship.

DATA AVAILABILITY

The data that support the findings of this study are available from the corresponding author upon reasonable request.

REFERENCES

- P. R. Roelfsema, H. Shibai, L. Armus, D. Arrazola, M. Audard, M. D. Audley, C. M. Bradford, I. Charles, P. Dieleman, Y. Doi, L. Duband, M. Eggers, J. Evers, I. Funaki, J. R. Gao, M. Giard, A. di Giorgio, L. M. G. Fernández, M. Griffin, F. P. Helmich, R. Hijmering, R. Huisman, D. Ishihara, N. Isobe, B. Jackson, H. Jacobs, W. Jellema, I. Kamp, H. Kaneda, M. Kawada, F. Kemper, F. Kerschbaum, P. Khosropanah, K. Kohno, P. P. Kooijman, O. Krause, J. van der Kuur, J. Kwon, W. M. Laauwen, G. de Lange, B. Larsson, D. van Loon, S. C. Madden, H. Matsuhara, F. Najarro, T. Nakagawa, D. Naylor, H. Ogawa, T. Onaka, S. Oyabu, A. Poglitsch, V. Reveret, L. Rodriguez, L. Spinoglio, I. Sakon, Y. Sato, K. Shinozaki, R. Shipman, H. Sugita, T. Suzuki, F. F. S. van der Tak, J. T. Redondo, T. Wada, S. Y. Wang, C. K. Wafelbakker, H. van Weers, S. Withington, B. Vandenbussche, T. Yamada, and I. Yamamura, *Publ. Astron. Soc. Aust.* **35**, e030 (2018); [arXiv:1803.10438](https://arxiv.org/abs/1803.10438).
- D. H. Martin and E. Puppelt, *Infrared Phys.* **10**, 105 (1970).
- M. Vaughan, *The Fabry-Perot Interferometer: History, Theory, Practice and Applications* (A. Hilger, 2017), p. 583.
- E. Hecht, *Optics*, 4th ed. (Addison-Wesley, 2002).
- P. E. Clegg, P. A. R. Ade, J. A. Long, D. Lorenzetti, S. Molinari, A. G. Murray, D. A. Naylor, B. Nisini, K. Norman, A. Omont, R. Orfei, T. J. Patrick, D. Péquignot, D. Pouliquen, M. C. Price, N.-Q. Rieu, A. J. Rogers, F. D. Robinson, M. Saisse, P. Saraceno, G. Serra, S. D. Sidher, A. F. Smith, H. A. Smith, L. Spinoglio, B. M. Swinyard, D. Texier, W. A. Towlson, N. R. Trams, S. J. Unger, and G. J. White, *Astron. Astrophys.* **315**, L38 (1996).
- J. M. Green, *J. Phys. E: Sci. Instrum.* **13**, 1302 (1980).
- A. Poglitsch, J. W. Beeman, N. Geis, R. Genzel, M. Haggerty, E. E. Haller, J. Jackson, M. Rumitz, G. J. Stacey, and C. H. Townes, *Int. J. Infrared Millimeter Waves* **12**, 859 (1991).
- P. A. R. Ade, G. Pisano, C. Tucker, and S. Weaver, *Proc. SPIE* **6275**, 62750U (2006).
- See <https://c-flex.com/> for C-Flex Bearing Co., Inc., 2015; Online accessed 04 June 2020.
- R. Huisman, J. W. G. Aalders, M. J. Eggers, J. Evers, H. M. Jacobs, B. J. van Leeuwen, A. C. T. Nieuwenhuizen, G. R. Ploeger, K. J. Wildeman, B. Jayawardhana, and J. M. A. Scherpen, *Mechatronics* **21**, 1259 (2011).
- G. L. Pilbratt, J. R. Riedinger, T. Passvogel, G. Crone, D. Doyle, U. Gageur, A. M. Heras, C. Jewell, L. Metcalfe, S. Ott, and M. Schmidt, *Astron. Astrophys.* **518**, L1 (2010).
- G. R. Davis, I. Furniss, W. A. Towlson, P. A. R. Ade, R. J. Emery, W. M. Glencross, D. A. Naylor, T. J. Patrick, R. C. Sidey, and B. M. Swinyard, *Appl. Opt.* **34**, 92 (1995).
- G. Makiwa, “Performance characterization of a millimeter-wave photomixer,” M.Sc. thesis, Department of Physics and Astronomy, University of Lethbridge, Lethbridge, AB, 2011.
- I. Veenendaal, D. Naylor, B. Gom, S. Gunuganti, C. Winter, M. Jones, and D. Walker, *Proc. SPIE* **9904**, 99045E (2016).
- I. Veenendaal, “A cryogenic test facility,” M.Sc. thesis, Department of Physics and Astronomy, University of Lethbridge, Lethbridge, AB, 2016.
- C. A. Palmer and E. G. Loewen, *Diffraction Grating Handbook*, 6th ed. (Newport Corporation, New York, 2005).
- D. A. Naylor, B. G. Gom, P. A. R. Ade, and J. E. Davis, *Rev. Sci. Instrum.* **70**, 4097 (1999).
- See <https://www.phytron.eu/> for Phytron GmbH, 2017; Online accessed 04 June 2020.
- T. Middellmann, A. Walkov, G. Bartl, and R. Schödel, *Phys. Rev. B* **92**, 174113 (2015); [arXiv:1507.06822](https://arxiv.org/abs/1507.06822).
- B. J. Frey, D. B. Leviton, and T. J. Madison, *Proc. SPIE* **6273**, 62732J (2006).
- E. V. Loewenstein, D. R. Smith, and R. L. Morgan, *Appl. Opt.* **12**, 398 (1973).
- I. Veenendaal, B. Gom, D. A. Naylor, and A. Christiansen, *Proc. SPIE* **10539**, 105390T (2018).